Title

A photoactivable multi-inhibitor nanoliposome for tumour control and simultaneous inhibition of treatment escape pathways.

Journal

Nature nanotechnology, 11(4)

ISSN

1748-3387

Authors

Spring, Bryan Q
Bryan Sears, R
Zheng, Lei Zak
et al.

Publication Date

2016-04-01

DOI

10.1038/nnano.2015.311

Peer reviewed

Published in final edited form as:

Nat Nanotechnol. 2016 April ; 11(4): 378–387. doi:10.1038/nnano.2015.311.

A photoactivable multi-inhibitor nanoliposome for tumour control and simultaneous inhibition of treatment escape pathways

Bryan Q. Spring[1,2,†], **R. Bryan Sears**[1,3,†], **Lei Zak Zheng**[1,†], **Zhiming Mai**[1], **Reika Watanabe**[4], **Margaret E. Sherwood**[1], **David A. Schoenfeld**[5], **Brian W. Pogue**[6], **Stephen P. Pereira**[7], **Elizabeth Villa**[4], and **Tayyaba Hasan**[1,8,*]

[1]Wellman Center for Photomedicine, Massachusetts General Hospital and Harvard Medical School, Boston, MA 02114

[2]Department of Physics, Northeastern University, Boston, MA 02115

[3]Department of Chemistry, Emmanuel College, Boston, MA 02115

[4]Department of Chemistry and Biochemistry, University of California San Diego, La Jolla CA 92093

[5]Massachusetts General Hospital and Harvard University, Biostatistics Unit, Boston MA 02114

[6]Thayer School of Engineering, Dartmouth College, Hanover, NH 03755

[7]UCL Institute for Liver and Digestive Health, University College London, Royal Free Hospital Campus, London NW3 2QG, UK

[8]Division of Health Sciences and Technology, Harvard University and Massachusetts Institute of Technology, Cambridge, MA 02139

Abstract

Nanoscale drug delivery vehicles can facilitate multimodal therapies of cancer by promoting tumour-selective drug release. However, few are effective because cancer cells develop ways to resist and evade treatment. Here, we introduce a photoactivatable multi-inhibitor nanoliposome (PMIL) that imparts light-induced cytotoxicity in synchrony with photo-initiated and sustained release of inhibitors that suppress tumour regrowth and treatment escape signalling pathways. The

*Correspondence and requests for materials should be addressed to T.H., ; Email: thasan@mgh.harvard.edu
†These authors contributed equally to this work.

Author contributions

B.Q.S., R.B.S., L.Z.Z., and T.H. conceived and designed experiments. B.Q.S., R.B.S., L.Z.Z., Z.M., R.W., M.E.S., and E.V. performed experiments. R.B.S. synthesized the nanomaterials. B.Q.S., R.B.S. and E.V. developed methodology and performed data analysis. D.A.S. contributed to statistical analysis of the data. B.Q.S., R.B.S., L.Z.Z., and T.H. prepared the manuscript. B.W.P., S.P.P. and E.V. contributed to experimental design and manuscript preparation. All authors contributed to editing the final manuscript.

Supplementary information accompanies this paper at www.nature.com/naturenanotechnology.

Competing financial interests

The authors declare no competing financial interests.

PMIL consists of a nanoliposome doped with a photoactivatable chromophore (benzoporphyrin derivative, BPD) in the lipid bilayer, and a nanoparticle containing cabozantinib (XL184)—a multikinase inhibitor—encapsulated inside. Near infrared tumour irradiation, following intravenous PMIL administration, triggers photodynamic damage of tumour cells and microvessels, and simultaneously initiates release of XL184 inside the tumour. A single PMIL treatment achieves prolonged tumour reduction in two mouse models and suppresses metastatic escape in an orthotopic pancreatic tumour model. The PMIL offers new prospects for cancer therapy by enabling spatiotemporal control of drug release whilst reducing systemic drug exposure and associated toxicities.

Nanoscale drug delivery systems enable controlled drug release with increased tumour selectivity and reduced toxicity[1]. Recently, multifunctional nanoparticles activated by external stimuli have emerged to enhance tumour-selective drug release[1]. These activatable delivery vehicles include optically responsive nanomaterials that support a broad range of biophotonic therapy and imaging applications[2–4], offering great promise for facilitating multimodal therapies of cancer. However, a fundamental challenge in oncology is that a number of resistance mechanisms and escape pathways ultimately limit treatment efficacy[5,6].

Here, we report near infrared (NIR) light-activated PMILs that impart photocytotoxicity to multiple tumour compartments and enable photo-initiated, sustained release of a multimolecular inhibitor with potent antiangiogenic activity and suppression of prominent treatment escape pathways (Fig. 1a). This unique approach impairs multiple, distinct molecular targets and is motivated by a three-way mechanistic interaction to combine: *(i)* photodynamic therapy (PDT)-induced tumour cell apoptotic signalling with XL184 inhibition of anti-apoptotic signalling pathways that promote cell survival; *(ii)* PDT-induced microvessel damage with sustained XL184 inhibition of vascular endothelial growth factor (VEGF) signalling to suppress tumour angiogenesis and vascular regrowth; and, *(iii)* exploiting a second molecular target of XL184, sustained inhibition of MET—the receptor tyrosine kinase for hepatocyte growth factor—signalling to suppress cancer cell motility, invasion and metastatic escape in response to tumour hypoxia induced by vascular damage and antiangiogenic therapy[7,8]. We show that BPD–XL184 PMILs realize these complementary interactions, resulting in enhanced tumour reduction *in vivo* in two mouse models of human pancreatic ductal adenocarcinoma (PDAC). In contrast to the corresponding monotherapies and combination therapy using conventional drug formulations, a single treatment cycle using PMILs results in prolonged local tumour control in a subcutaneous and in an orthotopic PDAC mouse model.

VEGF and MET are prime examples of tumour signalling pathways that promote treatment escape. VEGF and its receptors (e.g., VEGFR2) represent key targets for antiangiogenic therapy, and up-regulation of VEGF signalling has been observed in response to radiotherapy[9], chemotherapy[10], cytoreductive surgery[11], and PDT[12,13]. MET is frequently expressed by cancer stem-like cells thought to drive tumour recurrence[14], and abnormal MET signalling has been shown to promote the epithelial-mesenchymal transition[15], cancer cell stemness[15] as well as tumour growth, invasion and metastasis[5,15]. Moreover, MET

signalling is also observed in response to anti-VEGF therapy and comprises a prominent escape mechanism from antiangiogenic treatments[5]. When the tumour vasculature is pruned by anti-VEGF therapy, the hypoxic tumour microenvironment stimulates MET expression[7,8,16]. McDonald and colleagues elegantly demonstrated that concurrent inhibition of the VEGF and MET signalling pathways results in the favourable benefits of antiangiogenic therapy in slowing tumour growth while mitigating the unwanted consequences of increased intratumoural hypoxia—cancer cell migration and tumour growth along remaining, functional vessels as well as via lymphatic routes[16,17]. Here, we demonstrate that PDAC tumours transiently up-regulate MET signalling in response to PDT *in vivo* (Supplementary Fig. 1), which closes the triangle to motivate a three-way interactive therapy (Fig. 1b)—suggesting a compelling rationale to combine concurrent anti-VEGF and -MET therapy with PDT—and motivated development of the PMIL.

This approach—utilizing liposomes loaded with a lipophilic therapeutic agent and encapsulating a PLGA nanoparticle that releases a second, complementary agent—is supported by the reported successes of nanoliposome-based delivery of chemotherapeutics[18,19] (Supplementary Note 1). An advantage of this hybrid drug delivery vehicle is that its lipid[18] and polymer components[20,21] are all in clinical use and are biodegradable, nontoxic chemicals that can be metabolized by the body. PMILs build on these advances by utilizing light activation not only for photodynamic action but also as a drug release mechanism to enable tumour-focused, spatiotemporally synchronized combination therapies. This opens the door to a number of combination therapies for which capturing and suppressing bursts in molecular signalling dynamics is key.

PMIL design, synthesis and characterization

PMILs were synthesized with the lipophilic photosensitizer BPD formulated within the lipid bilayer of a liposome encapsulating PLGA nanoparticles[20,21] loaded with the hydrophobic multikinase inhibitor XL184 (Figs. 2a–c). The NP[XL184] was engineered to optimize the XL184 loading efficiency (Supplementary Fig. 2) and to be smaller in diameter than the liposomes (Figs. 2d,e) in order to facilitate its encapsulation within the liposome. In this design, the lipid bilayer acts to protect NP[XL184] from solvent exposure, limiting hydrolysis and systemic XL184 release prior to photo-induced drug release (Figs. 2f,g and Supplementary Fig. 3). We reasoned that NIR irradiation (using a 690 nm laser matched to BPD absorption) could deposit enough photonic energy to promote BPD-mediated photochemistry at the lipid bilayer and disrupt the integrity of the liposome[4,22] (Supplementary Note 2), thereby exposing the NP[XL184] to solvent and accelerating the liberation of the payload in the target lesion (Fig. 2f). Reactive oxygen species scavengers significantly suppressed photo-induced XL184 release indicating the involvement of photochemical drug release (Fig. 2f and Supplementary Fig. 4). The 50:50 PLGA ratio used to synthesize the NP[XL184] is designed for sustained XL184 delivery over a period of several days, with an initial burst release upon liposome disruption and water contact that is followed by a slower, sustained release phase due to nanoparticle erosion and XL184 diffusion (Fig. 2f)[20]. In contrast, XL184 is released from the PMIL over a period of several weeks in the absence of photo-induced release (Fig. 2f). Electron microscopy indicates a NP[XL184] encapsulation efficiency of ~20% within liposomes (Figs. 3a–c and

Supplementary Fig. 5) and disruption of the bilayer following laser irradiation (Figs. 3d,e and Supplementary Fig. 5). Surprisingly, although the majority of NP[XL184] is unencapsulated by a lipid bilayer, light activated drug release is prominent and might be explained by self-assembly of lipid monolayers onto PLGA nanoparticles (Supplementary Note 3).

Upon photo-release, XL184 is liberated to initiate inhibition of multiple kinases (Supplementary Note 4). XL184 is approved by the US Food and Drug Administration for treatment of patients with medullary thyroid cancer, based on a promising phase III trial[23], and is currently in clinical trials for PDAC (NCT01663272) as well as for a number of other malignancies. Because XL184 inhibits escape of anti-VEGF therapy via MET signalling[16] and inhibits pancreatic cancer stem-like cells[14,24], XL184 offers promise for treatment of PDAC in comparison to the poor phase III results for using anti-VEGF therapy alone in combination with gemcitabine[25].

In addition to photo-release of NP[XL184], NIR irradiation also triggers BPD-PDT to directly damage microvasculature, cancer cells or both, depending on the time of illumination following BPD administration[26–28]. As an example, BPD-PDT is used routinely in the clinic for selective closure of choroidal neovasculature associated with age-related macular degeneration while sparing the overlying neurosensory retina to preserve visual acuity[29]. For oncological applications, BPD-PDT is often most effective at time points that balance BPD localization in neovasculature with extravasation into the tumour parenchyma (60–90 minutes post-injection), which induces both microvasculature and cancer cell destruction[26]. In a promising phase I/II clinical trial (VERTPAC), such a BPD-PDT regimen produced a 1–4 cm zone of tumour necrosis with a 100% patient response rate for light delivered via optical fibers positioned percutaneously within locally advanced PDAC tumours under computed tomography guidance[30]. Moreover, the unique mechanisms of cell death induced by PDT[31,32]—including direct damage to Bcl-2 protein (a major anti-apoptotic factor and mediator of drug-resistance) and mitochondrial cytochrome c release (a potent pro-apoptotic signal)—are effective against chemo- and radioresistant cells[33–35] and sensitize cancer cells to chemotherapeutics[33,34] as well as to molecular inhibitors[12,36].

BPD is nontoxic (Supplementary Note 5), however, XL184 possesses significant toxicities that can require concomitant medications, dose interruption or dose reduction[23]. To limit the need for chronic XL184 administration and its systemic exposure to the body, the PMIL was designed to realize tumour-focused release of XL184.

Cellular PMIL internalization and *in vitro* efficacy

Cellular uptake of PMILs and of liposomes loaded with BPD in the bilayer but lacking XL184, L[BPD], was determined by BPD fluorescence confocal microscopy in monolayer cultures of AsPC1 cells derived from metastatic human PDAC ascites (VEGR1$^+$ and MET$^+$ with multiple oncogenic mutations; Supplementary Note 6). Both the PMIL and the L[BPD] underwent cellular internalization (Fig. 4a), with similarity to the pharmaceutical formulation of BPD[35]. BPD-PDT of AsPC1 cells using either L[BPD] or PMILs results in increased MET activation (Figs. 4b,c and Supplementary Fig. 6). PDT-induced MET

activation is down regulated using scavengers of reactive oxygen species produced by PDT photochemistry or by inhibiting epidermal growth factor receptor (EGFR)-mediated transactivation of MET (Fig. 4b and Supplementary Note 7). To investigate MET inhibition upon PMIL uptake into cancer cells, and photo-induced release of XL184, western blotting was used to measure phosphorylated MET (pMET; activated MET) as well as total MET expression for untreated AsPC1 cells versus cells treated with L[BPD] or PMILs that received a sub-lethal dose of NIR light (1 J·cm $^{-2}$) after a 1 h incubation period (Fig. 4c). BPD-PDT using L[BPD] results in enhanced MET phosphorylation while PMILs suppress MET activation (Fig. 4c). In the absence of photo-induced XL184 release, the PMILs have no effect on the basal pMET level (Fig. 4c). These results indicate that NIR irradiation triggers XL184 release from the PMIL such that the initiation of MET inhibition coincides with photodynamic cytotoxicity. Note that in contrast to photoinduced suppression of MET activation, none of the treatment arms had a significant impact on the total MET level.

Harnessing this photo-induced release of XL184 from PMILs, we hypothesized that simultaneous photocytotoxicity and inhibition of MET activation—and, thereby, suppression of downstream anti-apoptotic survival pathways[14]—could enhance cancer cell death. Note that XL184 also inhibits other receptor tyrosine kinases involved in intra- and autocrine cancer cell signalling, such as VEGFR1 (Supplementary Note 4). Cancer cell death was probed for the following treatments (250 nM BPD and/or 100–125 nM XL184) administered to AsPC1 cells: XL184; NP[XL184]; L[BPD]; co-administration of L[BPD] and NP[XL184] as separate agents; and, PMIL. The submicromolar doses of XL184 used here do not induce cancer cell death as a single agent (Fig. 4d; Supplementary Note 8). NIR photoirradiation (690 nm) was performed for a range of light doses (0–10 J·cm^{-2}) 1 h post drug administration. L[BPD]- and PMIL-PDT showed a characteristic increase in cell killing with increasing light dose with no dark toxicity. Furthermore, MET inhibition using PMILs induces an enhanced level of cancer cell death in comparison to L[BPD]-PDT as well as in comparison to co-administration of L[BPD] and NP[XL184] as separate agents (Fig. 4d). Collectively, these *in vitro* cancer cell culture studies indicate that inhibition of kinase activation simultaneous with photocytotoxicity can enhance cancer cell death.

PMIL efficacy in two mouse models of pancreatic cancer

The suppression of MET activation and modest enhancement of cancer cell cytotoxicity using the PMIL *in vitro* is promising for *in vivo* application. *In vivo*, the PMIL acts not only on cancer cells but also on paracrine receptor tyrosine kinase signalling, the tumour vasculature, tumour cell motility and metastatic escape, with potential to provide further gains in efficacy compared to conventional drug formulations. For instance, XL184 acts on endothelial cells lining tumour blood[16] and lymphatic[17] vessels (e.g., via VEGFR inhibition). To assess the efficacy of PMILs in controlling localized tumours *in vivo*, we performed a single treatment cycle in established xenograft tumours (~50 mm^3 in size) 18 d following subcutaneous implantation of AsPC1 cells in mice. A single intravenous administration of the following treatments was given to the randomized mice: no-treatment control; XL184; NP[XL184]; L[BPD]; co-administration of L[BPD] and NP[XL184] as separate agents; and, PMIL. Each formulation contained 0.25 mg·kg^{-1} of BPD and/or 0.1–0.125 mg·kg^{-1} XL184. Here, NIR irradiation was performed 1 h following injection—via

transcutaneous illumination of the tumour—to induce both vascular and cancer cell destruction. In contrast to continued tumour growth observed for XL184 and BPD-PDT monotherapy, PMIL-mediated combination therapy exhibited a pronged reduction in tumour volume over 10 d following a single treatment (Fig. 5a). Compared to the no-treatment control group, the mean tumour reduction following PMIL treatment was 92% (day 37; Fig. 5b). This result contrasts with the monotherapy controls and the combination therapy by conventional co-administration of L[BPD] and NP[XL184] as separate agents—all of which showed marginal anti-tumour effects as a trend in slowing tumour growth but did not achieve a significant reduction in tumour volume (Fig. 5a,b).

To investigate toxicity, metastasis and microvascular effects, and to further probe local tumour control in an additional tumour model using PMILs, we next investigated the same treatment arms in a metastatic mouse model by implanting PDAC cells into the pancreas. Mouse weight was monitored before (day 10 post-tumour inoculation) and after (day 24) treatment as a metric of toxicity (Fig. 5c). The gain in mouse weight and 100% survival of the mice through the treatment endpoint (day 24) indicate that PDT combined with low dose XL184 treatment has low toxicity (Fig. 5c). Furthermore, pancreatic tumour volumes and histopathology (Supplementary Fig. 8) assessed at the treatment endpoint (day 24) corroborate the enhanced local control of the primary tumour as found in the subcutaneous model for PMILs (Fig. 5d).

These orthotopic pancreatic tumours are hypovascular in comparison to the surrounding pancreatic tissue (Figs. 6a,b). Nevertheless, XL184 ($P = 0.19$, Mann-Whitney U test) and PMIL-treatment ($P = 0.20$, Mann-Whitney U test) selectively induced trends in reduced intratumoural—but not peritumoural—microvessel density versus the no-treatment control tumours (Fig. 6b). Because of the substantial degree of tumour shrinkage by PMILs (Fig. 5d), which tends to compact remaining vasculature and to obscure interpretation of microvessel density[37], we also estimated the intratumoural microvessel volume using an immunofluorescence and digital slide scanning microscopy technique to efficiently sample the endothelial cell content of entire tumour volumes[38] (*Methods* and Supplementary Note 9). The intratumoural microvessel volume estimate revealed a significant reduction in total tumour microvascularity achieved by the PMIL, which suggests an antivascular effect facilitated by PDT with suppression of vascular and tumour regrowth by sustained XL184 release. Furthermore, invasive tumour borders and metastatic infiltrates within the surrounding pancreatic tissue characterize this orthotopic model of PDAC (Fig. 6a). Metastases in the liver and retroperitoneal lymph nodes appear rapidly in this model, as assessed by a quantitative polymerase chain reaction assay (*Methods*) that measures the number of viable, human metastatic cancer cells in organ biopsies (Fig. 6d). The single PMIL treatment achieved a 98.7% mean reduction in liver and retroperitoneal lymph node metastasis compared to the no-treatment control group at the treatment endpoint (day 24), while the other treatment groups did not achieve a statistically significant change in metastasis (Fig. 6d).

The local tumour reduction and suppression of metastasis resulting from a single PMIL treatment contrasts with the use of XL184 as a single agent, which is given daily over an extended period by oral administration. For instance, Sennino *et al.* reported 99% primary

tumour reduction, 79% microvessel density reduction and 100% liver metastasis reduction in a mouse model of pancreatic neuroendocrine tumours (40 mg·kg^{-1} XL184, administered daily for 3 wks)[16]. Here, a single PMIL treatment (including 0.1–0.125 mg·kg^{-1} XL184) achieved 92% and 61% reductions of subcutaneous and orthotopic PDAC tumours, respectively, with 70% intratumoural microvessel volume reduction and 99% metastatic cancer cell reduction in the liver and regional lymph nodes. Remarkably, the interaction of PDT with photo-initiated and sustained XL184 release facilitated by the PMIL enables the same therapeutic efficacy of daily oral XL184 monotherapy with less than a thousandth (~1/6,700th) of the XL184 dosage (Supplementary Note 10). This indicates that the PMILs offer a significant potential to reduce systemic exposure to XL184, reducing risks of toxic side effects and the need for dose interruptions.

The *in vivo* efficacy PMIL also contrasts strongly with co-administration of L[BPD] and NP[XL184] as separate agents. The PMIL unites the pharmacokinetics of L[BPD] and NP[XL184] delivery and enables tumour-confined, photo-induced XL184 release, while the conventional delivery of L[BPD] and NP[XL184] precludes a full interaction between these therapies. The enhanced efficacy of the PMIL highlights the importance of co-packaging interactive therapeutic agents into one carrier with spatiotemporally synchronized release. Note that although XL184 had no cytotoxicity as a single agent *in vitro* (Fig. 4d) that PMIL treatment achieved super-additive cancer cell killing both *in vitro* and *in vivo* (Supplementary Fig. 7), which suggests a synergistic interaction between XL184 and BPD-PDT facilitated by the PMIL (Supplementary Note 11). The requirement for co-packaging to achieve maximal impact is likely due to rapid (within 1–4 h) microvessel damage and shutdown by both XL184[39] and BPD[27] that mutually compromise co-delivery of these therapies as separate agents using conventional drug delivery formulations. The rapid vascular effects of PDT in particular (<1 h for blood flow stasis onset with a duration >48 h[27]) would preclude XL184 delivery during the critical time window for anti-apoptotic signalling and vascular regrowth inhibition during the burst in tumour VEGF (within 6 h[40]) and MET (within 72 h; Supplementary Fig. 1) signalling that follows cytotoxic therapy. Rapid PDT-induced vascular shutdown would inhibit overall XL184 delivery (55 h half-life) whereas nanoparticles entrapped in the tumour release XL184 locally for a sustained period to inhibit vascular regrowth and metastasis following PDT. XL184 could be administered prior to PDT but this still precludes sustained therapeutic doses of XL184 until tumour vascular regrowth following PDT.

Conclusions

In summary, the complexities of cancer necessitate the innovation of drug delivery platforms capable of addressing multiple tumour compartments as well as treatment escape mechanisms. An emerging paradigm in cancer therapy suggests that gains in local tumour control can be compromised by co-activation of multiple tumour survival signalling pathways that promote increased invasiveness and metastasis[5,8]. This aggressive response to treatment may ultimately limit patient survival. Combination therapies hold great promise for overcoming this paradox by addressing mechanisms of tumour recurrence and treatment escape. However, co-activation of multiple tumour survival signalling pathways and microvessel shutdown limit the efficacy of sequential drug delivery. New drug delivery

systems are needed to facilitate combinations spanning cytotoxic, antivascular and anti-invasive mechanisms. To address these challenges, we developed PMILs that integrate the antivascular and antiangiogenic mechanisms of photodynamic and anti-VEGF therapy while blocking tumour cell invasion, metastasis and escape via the MET pathway. This approach is inspired by recent advances in photoactivated nanomaterials[2,4], multi-drug loaded[41] as well as stimuli-responsive liposomes[42] and by the nanocell platform[43], which introduced extrinsically-activated drug release, maintenance of synergistic drug ratios and temporal targeting of distinct tumour compartments, respectively. PMILs utilize these features for multi-agent co-delivery with photo-release and entrapment of NP[XL184] within the tumour following vascular shutdown for sustained release. This approach uniquely enables a tumour-confined, spatiotemporally synchronized multi-modal combination therapy at the "right time and right place". The PMIL attenuates metastatic outgrowth and escape but the photodynamic component is presently limited to localized tumours and further developments will be needed to address established, distal metastases. Note that XL184 is eventually released from the PMIL in the dark (Fig. 2f) such that established metastases will be impacted by passive tumour accumulation of PMILs via the enhanced permeability and retention effect.

Future work will address models of advanced metastatic disease and will potentially involve further developments to incorporate targeted and activatable delivery for wide-field PDT with sufficient selectivity to treat disseminated micrometastases[44]. The role of the unencapsulated NP[XL184] population, and the possibility of a BPD-loaded lipid monolayer that contributes to light-activated therapy, will also be the subject of future studies. Alternatively, it is possible that the encapsulated NP[XL184] is the dominant contributor such that further reduction in the XL184 dose and systemic toxicity may be achieved by purification of encapsulated NP[XL184]. Collectively, the present study demonstrates that PMILs maximize therapeutic efficacy per treatment cycle and further studies are warranted to investigate long-term impacts on cure rate, survival and potentiation of standard chemotherapy regimens. The on-going phase II-III studies of PDT in PDAC form a good basis for developing this approach further.

METHODS

NP[XL184] synthesis and characterization

Prior to NP[XL184] synthesis, the biodegradable copolymer PLGA 50:50 (17 kDa; 0.18 $dL \cdot g^{-1}$; Lake Shore Biomaterials) was modified to incorporate a PEG moiety (COOH-PEG-NH_2; 3.5 kDa; JenKem Technology), which enhances both nanoparticle stability and circulation time[18]. Synthesis was then performed by nanoprecipitation[45]. In order to achieve maximal XL184 loading, nanoparticles were synthesized with various XL184 (>99.0% purity; Selleck Chemicals) and PEG-PLGA drug/polymer ratios ranging from 1–10% (w/w). Of the tested ratios, the XL184 molar loading efficiency was maximal at a drug/polymer (w/w) ratio of 1% (Supplemental Figure 2). In addition, a range of solvent:water ratios (1:2–1:10) were tested and the optimal ratio for NP[XL184] formation was 1:3 acetone:water. For the optimized synthesis protocol, XL184 was co-solubilized in 1 mL of acetone with PLGA-PEG at a 1% (w/w) drug to polymer concentration. Nanoprecipitation was achieved by

adding this mixture drop-wise using a 27½-gauge needle to 3 mL of H_2O stirred magnetically at 400 rpm. The reaction mixture was then stirred uncovered for 6 h to allow acetone evaporation, passed through a 0.2 μm filter and purified by ultrafiltration (Amicon-Millipore; 30 kDa cut-off) at 2500 rpm for 10 min with intermittent washing (4 cycles; 4 mL phosphate-buffered saline per wash). The XL184–PLGA nanoparticle loading efficiency was determined by optical absorption measurements following solvation of the nanoparticles in dimethyl sulfoxide, using the formula: 100·(no. moles following purification/no. moles available for synthesis). All NP[XL184] size and charge measurements were made by dynamic light scattering (Malvern, Zetasizer Nano ZS).

PMIL synthesis and characterization

PMILs co-encapsulating BPD (verteporfin; VWR International) and NP[XL184] were prepared by modification of existing synthesis methods[43]. The lipids (DPPC, DOTAP, cholesterol, and DSPE-PEG; Avanti Polar Lipids) were each dissolved separately in chloroform, and then mixed together in a molar ratio of 2:0.2:1:0.2 (DPPC:DOTAP:cholesterol:DSPE-PEG) with 100 nmoles of BPD. This lipid composition was selected based on the previously reported pharmacological success of similar compositions[18]. Inclusion of the cationic lipid, DOTAP, resulted in a zeta potential (surface charge) of +3 mV. This slightly cationic surface charge promotes cellular uptake without significant cytotoxicity to maintain biocompatibility[46]. To form thin lipid films containing BPD, chloroform was removed by roto-evaporation and by placing the sample under vacuum overnight. Next, lipid film hydration was achieved by adding NP[XL184] (50 nmoles of XL184) in 1 mL of phosphate-buffered saline. To ensure adequate encapsulation of NP[XL184], the thin film was subjected to 10 freeze-thaw cycles (6 min per cycle) at 0°C and 45°C, below and above the highest transition temperature of the lipid mixture (DPPC; T_m = 41°C). The resulting dispersion of multilamellar liposomes was extruded through a 200-nm-diameter polycarbonate membrane using a mini-extruder system (Avanti Polar Lipids) to form unilamellar liposomes. BPD and XL184 not loaded into the PMIL were removed by dialysis (Spectra/Por; 300 kDa cut-off; 1 mL sample in 4 L of phosphate-buffered saline at 4°C for 18 h). During the dialysis period, the sample was analysed by dynamic light scattering measurements. Initially, these measurements indicated a bimodal distribution with peaks at 80 nm (NP[XL184]) and 150 nm (PMIL), which gradually became a single monodispersive peak (PDI < 0.2) as purification of the PMILs completed. However, electron microscopy revealed the presence of residual NP[XL184] not incorporated within liposomes within the PMIL samples (Supplementary Note 3). The PMIL BPD and XL184 concentrations and loading efficiencies were determined by fluorescence and absorbance spectroscopy or by high-performance liquid chromatography (Hydrosil C18 ODS; 2.0 cm × 14.0 cm; 50% acetonitrile in H_2O → 100% acetonitrile; 0.5 h), respectively, following solvation of the PMILs in dimethyl sulfoxide. All PMIL size and charge measurements were made by dynamic light scattering (Malvern, Zetasizer Nano ZS). L[BPD] was synthesized analogously to the PMIL, but without NP[XL184].

PMIL stability and drug photo-release kinetics

PMIL and NP[XL184] size stability during storage at 4°C was investigated by repeated dynamic light scattering measurements over a period of 40 d (Supplementary Fig. 3). Dark

release and photoinduced drug release were measured using dialysis membranes in phosphate-buffered saline at 37°C with 10% fetal bovine serum added to each dialysis tube (Spectra/Por; NP[XL184], 100 kDa cut-off; PMILs, 300 kDa cutoff; Fig. 2f). A 690 nm diode laser (High Power Devices, Inc.) was used for all NIR irradiation experiments. During dialysis samples were collected periodically and placed immediately in acetonitrile containing 1% of the internal standard *N*-(1-naphthyl)ethylenediamine. Separation and quantification of drug components was achieved by liquid chromatography-tandem mass spectrometry (LC-MS/MS) using standard curves for each drug normalized to the internal standard. Briefly, 1.0 μL of dialysis sample was injected into a ZorbaxC18 (2.1 × 50 mm) column eluted at 0.400 mL/min with acetonitrile and 10 mM ammonium formate (80% → 20% over 4 min). Detection of drug components was made using triple quadrupole MS/MS detection with an ion source ESI+ in MRM scan mode to identify the product ions for BPD (ret. time = 4.12 min, 513 m/*z*) and XL184 (ret. time= 2.68 min, 232 m/*z*). Quantitative analysis of chromatograms allowed for area under curve integrations of each product ion normalized to the internal standard (ret. time 1.20 min; 170 m/*z*). Total moles were determined using standard curves and percent loss calculated for each time point after correcting for sample volume changes. The resulting BPD and XL184 release profiles were fit individually to a simple one- or two-phase exponential model: $a_0 + a_1 \cdot e^{-k_1 \cdot t} + a_2 \cdot e^{-k_2 \cdot t}$, where a_0 is an offset, a_1 and a_2 are the maxima release plateaus (at equilibrium) of phases 1 and 2, k_1 and k_2 are the release rate constants of phases 1 and 2, and t is time from placing the sample in serum media within the dialysis tube. Note that XL184 release from NP[XL184] is sufficiently described by a single-phase model (P=0.067, two-phase alternative hypothesis), whereas XL184 release from the PMIL with or without laser irradiation is best described by the multi-phase model (P =0.0003–0.0079). Dynamic light scattering and transmission electron microscopy were also performed before and after photoirradiation (Fig. 3 and Supplementary Fig. 4).

Cryo-electron microscopy

Cryo-EM was performed using a FEI Technai G2 Polara microscope equipped with an energy filter (Gatan) and a K2 Summit direct detection device (Gatan). Briefly, 5 μL of nanomaterial sample (~60 μM BPD for the PMIL or L[BPD]; ~30 or 125 μM XL184 for the PMIL or NP[XL184], respectively) mixed with 2 μL of BSA Gold Tracer (EM-grade 6 nm; Electron Microscopy Sciences, 25484) re-suspended in phosphate-buffered saline were deposited onto glow-discharged holey carbon grids (QUANTIFOIL R 2/1 200 mesh, copper; Electron Microscopy Sciences), blotted and rapidly vitrified in a liquid ethane and propane mixture (50:50) using a custom-built plunger (Max Planck Institute of Biochemistry, Germany). Imaging was performed at 300 kV under low-dose conditions with 4.98 Å or 6.12 Å sampling and a defocus of −3 or −6 μm for 2D or 3D images, respectively. 2D images were obtained using the dose-fractionation mode of the detector (~20–40 e/Å^2 cumulative dose). Tilt series (±60°) for tomography were collected around a single axis with a 2° sampling increment using SerialEM software[47] (~100 e/Å^2 cumulative dose). Tomographic reconstructions were calculated using the IMOD tomography package[48]. Renders of 3D PMIL and NP[XL184] objects were created by manual segmentation in IMOD and rendered using VMD[49]. Manual particle counting was performed as described in Supplementary Fig. 5. Only unambiguous NP[XL184] objects were counted (~20 nm in diameter or greater).

Mean lamellarity was calculated as: $\Sigma_{\boldsymbol{L}}(\boldsymbol{N_L} \cdot \boldsymbol{L})/\Sigma_{\boldsymbol{L}}\boldsymbol{N_L}$, where $\boldsymbol{N_L}$ is the number of objects with lamellarity $\boldsymbol{L}$ (e.g., $\boldsymbol{L} = \mathbf{1}$ for unilamellar liposomes).

Transmission electron microscopy

TEM (Philips CM10) was performed using negative staining either on untreated (200 mesh nickel PELCO® Support Film with a Formvar/carbon coating, Ted Pella Inc.) or ionized carbon coated grids (to promote sample adhesion). Briefly, 10 μL of sample was added to the grid, air-dried and stained (2 μL, 1.0% phosphotungstic acid). Next, the grid was blotted dry and washed with 5 μL of dH_2O. Imaging was performed at 100.0 kV and magnifications of ~10,000–50,000×.

Cell culture studies

Monolayer cultures of AsPC1 cells (American Type Culture Collection, CRL-1682; low passage number, <20)—recently tested (July 2015) and found to be negative for mycoplasma contamination (MycoAlert mycoplasma detection kit, Lonza)—were maintained in media (RPMI 1640, Mediatech) supplemented with 10% fetal bovine serum (Invitrogen), 100 units/mL penicillin and 100 μg/mL streptomycin. The AsPC1 cell line has not been listed in the database of cross-contaminated or misidentified cell lines maintained by the International Cell Line Authentication Committee. Cellular uptake of PMILs and L[BPD] was tested in multi-well plates with coverslip bottoms (Greiner Bio-One) plated with AsPC1 cells allowed to attach and grow overnight. Nanoconstructs were added to the wells at staggered time points to reach a concentration of 100 nM BPD and to achieve varying incubation times at 37°C (15–90 min). Imaging was performed with an Olympus FV1000 confocal microscope with a 20 × 0.75 NA (numerical aperture) objective. BPD excitation was performed using a 405 nm diode laser with an emission spectrograph centred on the 696 nm BPD fluorescence emission peak. The laser, photomultiplier tube detector and pinhole settings, as well as brightness-contrast adjustment settings for display, were kept constant for all images. In addition, phase contrast images were collected during microscopy in order to focus on a high-density field of cells (not shown). Images were also collected for untreated cells (0 min) to quantify the autofluorescence background and to define a fluorescence intensity threshold that rejects 99.5% of the background signal. This intensity threshold was applied to all images to select pixels above the autofluorescence background (true BPD signal) for analysis. The resulting cellular uptake data was fit to a simple biexponential pharmacokinetic model: $a \cdot (e^{-k \cdot t} - e^{-j \cdot t})$, where k and j are the elimination and absorption rate constants, a is a coefficient dependent on the administered BPD dose as well as its bioavailability and t is time post-administration. For *in vitro* PDT, $0.25 \cdot 10^6$ AsPC1 cells were grown on a 35-mm culture dish for 24 h and incubated with nanoconstructs containing BPD (250 nM equivalent) and/or XL184 (100–125 nM equivalent) in 1 mL complete medium for 1 h. The incubation media was then replaced with 2 mL of fresh, complete media prior to photoirradiation. This removal of nanoconstructs not uptaken by cells prior to irradiation limits the release of XL184 and the generation of photocytotoxic species to intracellular and cell-associated nanoconstructs. Cell viability was measured using the MTT assay 24 h following light irradiation. Singlet Oxygen Sensor Green (SOSG; Molecular Probes) and D-mannitol (Sigma-Aldrich) were used to probe reactive oxygen species involvement in BPD-PDT-induce MET activation. Tyrphostin AG1478 (Sigma-

Aldrich) and bacterial toxin B (Toxin B, *Clostridium difficile* - Calbiochem, Millipore) were used to test for involvement of enzymes known to participate in MET transactivation. SOSG and mannitol were added to cells immediately prior to laser irradiation in fresh media and then removed immediately after PDT by a second media replacement step. AG1478 and toxin B were incubated with cells in fresh media for 30 min and 2 h, respectively, prior to laser irradiation and then removed immediately after PDT by a second media replacement.

In vivo mouse models and treatments

All animal experiments were conducted with approval and according to guidelines established by the Massachusetts General Hospital Institutional Animal Care and Use Committee. Experiments were carried out on 6-week-old male Swiss nude mice weighing 20–25 grams (Cox Breeding Laboratories). For tumour implantations and photoirradiation, animals were anesthetized with 84 $mg \cdot kg^{-1}$ ketamine and 12 $mg \cdot kg^{-1}$ xylazine. Tumours were implanted by injection of a 50 μL volume containing 10^6 AsPC1 cells in a 1:1 mixture of Matrigel (BD Biosciences) and culture media. Subcutaneous tumours were implanted above the hind leg and tumour volumes were estimated longitudinally by measuring the three tumour dimensions using a calliper and the hemi-ellipsoid formula: $volume = \pi \cdot L \cdot W \cdot H/6$, where L, W and H, are the tumour length, width and height. Note that here, H, represents the measured height of the hemi-elliptical tumour, which is half the height of a full ellipsoid. Eighteen days following cancer cell implantation, subcutaneous tumours reached volumes of ~50 mm^3 prior to the start of treatment. For orthotopic tumour implantation, animals were laid supine, a small left abdominal flank incision was made to exteriorize the pancreas and the cell suspension was injected into the pancreas. A small amount of 10% povidone/iodine was applied topically to the injection site. Then the incision was closed with 4-0 sutures and 10% povidone/iodine was then applied to the incision site to prevent infection. Ten days after cancer cell implantation, orthotopic pancreatic tumours reached volumes of ~25 mm^3 prior to the start of treatment. All injections for treatment were done intravenously (tail vein) in 200 μL sterile phosphate-buffered saline. Mice were randomized into the various treatment groups, and the tumours of mice receiving BPD were irradiated with NIR light (using the 690 nm diode laser listed above) 1 h post-injection, delivered at an irradiance of 100 $mW \cdot cm^{-2}$. Subcutaneous tumours were irradiated transcutaneously while orthotopic tumours were surgically exposed as for tumour implantation and irradiated. Fourteen days after treatment, orthotopic tumours were excised to estimate their volumes using callipers and the ellipsoid formula: $volume = \pi \cdot L \cdot W \cdot H/6$.

Microvessel immunofluorescence imaging

Microvessel density and intratumoural microvessel volume were estimated as described previously[38]. Briefly, orthotopic pancreatic tumours were excised 2 weeks post-treatment, embedded in optimal cutting temperature compound and frozen at −80°C. A cryotome was used to cut 20-μm-thick cryosections. Sections were (1) fixed in 1:1 acetone:methanol for 15 minutes at −20°C, (2) air dried for 30 minutes, and (3) washed three times in phosphate-buffered saline. A blocking solution (Dako Protein Block Reagent) was applied for 30 minutes, followed by application of the immunostains, at ~5 μg/mL monoclonal antibody (MAb) each diluted in background reducing Dako Antibody Diluent for 2 h at room temperature in a humidifying chamber. Finally, the slides were washed again three times,

mounted (Invitrogen SlowFade Gold with 4′,6-diamidino-2-phenylindole, DAPI) with a coverslip and sealed with nail polish. Confocal fluorescence imaging was performed using an Olympus FluoView 1000 confocal microscope with a 10 × 0.4 numerical aperture (NA) or a 20× 0.75 NA objective. Excitation of DAPI, anti-mouse PECAM-1 (CD31; clone 390; CBL1337, Millipore) MAb-Alexa Fluor 568 conjugates and anti-human cytokeratin 8 (clone LP3K; MAB3156, R&D Systems) MAb-Alexa Fluor 647 conjugates was carried out using 405-, 559- and 635-nm lasers, respectively. Mosaic images of entire tumour cross-sections were collected and stitched together using the Olympus FluoView software. The anti-human cytokeratin 8 stain (a cytoskeletal protein highly expressed by AsPC1 cells) has dual selectivity for the epithelial cancer cells because it does not react with mouse proteins. All analyses were performed using custom MATLAB (Mathworks) routines for batch image processing[38]. Microvessel density values were calculated from whole tumour sections, within viable tumour tissue only, and averaged over slices from the entire tumour rather than a more complex “hot spot” identification and calculation, which is difficult to define objectively[38]. Intratumoural microvessel volume is calculated by multiplying microvessel density with the viable tumour volume in each slice and then summing over the whole tumour by interpolation[38]. Here, we used the minimum tumour subsampling necessary—based on a mathematical model—to resolve a statistically significant change in intratumoural microvessel volume, as validated previously using the orthotopic AsPC1 tumour model[38] (Supplementary Note 9).

Measurement of metastatic burden

A quantitative reverse transcription–polymerase chain reaction (qRT-PCR) assay was performed on excised liver and iliac lymph nodes to estimate the number of human cancer cells in excised organs as described and validated previously[44]. Briefly, qRT-PCR is used to measure the total number of human cancer cells from the level of human and mouse glyceraldehyde 3-phosphate dehydrogenase (GAPDH) housekeeping genes. At least 300 mg of freshly excised liver and retroperitoneal lymph nodes were collected at the treatment endpoint and snap frozen in liquid nitrogen. The frozen samples were then pulverized and homogenized, followed by RNA extraction (RNAeasy Plus Mini Kit; Qiagen). Human and mouse GAPDH gene were measured using custom synthesized primers (Invitrogen). For each specimen, the cycle threshold (*Ct*) from human GAPDH gene was normalized by *Ct* from mouse GAPDH gene. The normalized *Ct* was quantified into number of cancer cells using a standard curve generated with a set of organ lysates from no-tumour control mice mixed with different numbers of human cancer cells.

Statistical analyses

Specific statistical tests are indicated in the figure captions and were carried out using GraphPad Prism (GraphPad Software). All reported *P* values are two-tailed. Parametric tests (one-way ANOVA with Tukey’s post-test) were used for *in vitro* drug release (Fig. 2f and Supplementary Fig. 4) and *in vitro* cell culture (Figs. 4b,c,d and Supplementary Fig. 6) studies; and, the D’Agostino & Pearson omnibus normality test ($\alpha = 0.05$; requires $n \geq 8$ replicates per group) did not identify significant deviations from normality within these data sets (testing could only performed for groups with $n \geq 8$ replicates). Note that all groups within the drug release data were analysed together (some groups appear only in

Supplementary Fig. 4). Electron microscopy single-nanoparticle analysis (Figs. 3d) and all *in vivo* data (Figs. 5b,c,d, Figs. 6b,c,d and Supplementary Fig. 1) were analysed using nonparametric tests (the Mann-Whitney *U* test or Kruskal–Wallis one-way ANOVA). The Brown–Forsythe test ($\alpha = 0.05$) was applied to all data sets with $n \geq 3$ replicates to test for equal variance (regardless of whether parametric or nonparametric analysis was used) and identified significant deviations from equal variance (Figs. 3e, 5d and 6c). In these cases, the data were analysed following a logarithmic transform of the data to pass the Brown–Forsythe test. Two-way ANOVA was applied to test for synergistic treatment interactions[50] (Fig. 5d) following a natural logarithm transform of the data to pass the D'Agostino & Pearson omnibus normality test. No exclusion criteria were used, and no data points or animals were excluded from analysis. Investigators were not blinded to experimental groups unless noted otherwise. Animal sample sizes were selected to ensure adequate power (80%) to detect a 20% difference using a maximum of 16 animals per group assuming a standard deviation of 15%. For the subcutaneous model, significance was achieved with 5 animals per group.

Supplementary Material

Refer to Web version on PubMed Central for supplementary material.

Acknowledgments

We thank Nicki Watson (W. M. Kreck Microscopy Facility at the Whitehead Institute, Massachusetts Institute of Technology) for providing ionized carbon coated grids; Esther Oliva (Department of Pathology at Massachusetts General Hospital) for expert histopathologic review of tissue sections; Girgis Orbaid for a critical reading; and, Andrea Villanueva for assistance in preparing a 3D render of a PMIL cryo-EM tomogram. This work was supported by National Institutes of Health Grants RC1-CA146337 (to T.H.), R01-CA160998 (to T.H.), and P01-CA084203 (to B.W.P., S.P.P. and T.H.) and F32-CA144210 (to B.Q.S.).

References

1. Cheng Z, Al Zaki A, Hui JZ, Muzykantov VR, Tsourkas A. Multifunctional nanoparticles: cost versus benefit of adding targeting and imaging capabilities. Science. 2012; 338:903–910. [PubMed: 23161990]
2. Lovell JF, et al. Porphysome nanovesicles generated by porphyrin bilayers for use as multimodal biophotonic contrast agents. Nat Mater. 2011; 10:324–332. [PubMed: 21423187]
3. Cui S, et al. In vivo targeted deep-tissue photodynamic therapy based on near-infrared light triggered upconversion nanoconstruct. ACS Nano. 2013; 7:676–688. [PubMed: 23252747]
4. Carter KA, et al. Porphyrin-phospholipid liposomes permeabilized by near-infrared light. Nat Comms. 2014; 5:3546.
5. Sennino B, McDonald DM. Controlling escape from angiogenesis inhibitors. Nat Rev Cancer. 2012; 12:699–709. [PubMed: 23001349]
6. Holohan C, Van Schaeybroeck S, Longley DB, Johnston PG. Cancer drug resistance: an evolving paradigm. Nat Rev Cancer. 2013; 13:714–726. [PubMed: 24060863]
7. Pennacchietti S, et al. Hypoxia promotes invasive growth by transcriptional activation of the met protooncogene. Cancer Cell. 2003; 3:347–361. [PubMed: 12726861]
8. Pàez-Ribes M, et al. Antiangiogenic Therapy Elicits Malignant Progression of Tumors to Increased Local Invasion and Distant Metastasis. Cancer Cell. 2009; 15:220–231. [PubMed: 19249680]
9. Gorski DH, et al. Blockade of the vascular endothelial growth factor stress response increases the antitumor effects of ionizing radiation. Cancer Res. 1999; 59:3374–3378. [PubMed: 10416597]

10. Tran J, et al. A role for survivin in chemoresistance of endothelial cells mediated by VEGF. Proc Natl Acad Sci USA. 2002; 99:4349–4354. [PubMed: 11917134]
11. Justinger C, et al. Increased growth factor expression after hepatic and pancreatic resection. Oncol Rep. 2008; 20:1527–1531. [PubMed: 19020737]
12. Ferrario A, et al. Antiangiogenic treatment enhances photodynamic therapy responsiveness in a mouse mammary carcinoma. Cancer Res. 2000; 60:4066–4069. [PubMed: 10945611]
13. Solban N, et al. Mechanistic investigation and implications of photodynamic therapy induction of vascular endothelial growth factor in prostate cancer. Cancer Res. 2006; 66:5633–5640. [PubMed: 16740700]
14. Hage C, et al. The novel c-Met inhibitor cabozantinib overcomes gemcitabine resistance and stem cell signaling in pancreatic cancer. Cell Death Dis. 2013; 4:e627. [PubMed: 23661005]
15. Gherardi E, Birchmeier W, Birchmeier C, Vande Woude G. Targeting MET in cancer: rationale and progress. Nat Rev Cancer. 2012; 12:89–103. [PubMed: 22270953]
16. Sennino B, et al. Suppression of tumor invasion and metastasis by concurrent inhibition of c-Met and VEGF signaling in pancreatic neuroendocrine tumors. Cancer Discov. 2012; 2:270–287. [PubMed: 22585997]
17. Sennino B, Ishiguro-Oonuma T, Schriver BJ, Christensen JG, McDonald DM. Inhibition of c-Met reduces lymphatic metastasis in RIP-Tag2 transgenic mice. Cancer Res. 2013; 73:3692–3703. [PubMed: 23576559]
18. Drummond DC, Meyer O, Hong K, Kirpotin DB, Papahadjopoulos D. Optimizing liposomes for delivery of chemotherapeutic agents to solid tumors. Pharmacol Rev. 1999; 51:691–743. [PubMed: 10581328]
19. Davis ME, Chen ZG, Shin DM. Nanoparticle therapeutics: an emerging treatment modality for cancer. Nat Rev Drug Discov. 2008; 7:771–782. [PubMed: 18758474]
20. Makadia HK, Siegel SJ. Poly Lactic-co-Glycolic Acid (PLGA) as Biodegradable Controlled Drug Delivery Carrier. Polymers. 2011; 3:1377–1397. [PubMed: 22577513]
21. Hines DJ, Kaplan DL. Poly(lactic-co-glycolic) acid-controlled-release systems: experimental and modeling insights. Crit Rev Ther Drug Carrier Syst. 2013; 30:257–276. [PubMed: 23614648]
22. Thompson DH, Gerasimov OV, Wheeler JJ, Rui Y, Anderson VC. Triggerable plasmalogen liposomes: improvement of system efficiency. Biochim Biophys Acta. 1996; 1279:25–34. [PubMed: 8624357]
23. Elisei R, et al. Cabozantinib in progressive medullary thyroid cancer. J Clin Oncol. 2013; 31:3639–3646. [PubMed: 24002501]
24. Li C, et al. c-Met is a marker of pancreatic cancer stem cells and therapeutic target. Gastroenterology. 2011; 141:2218–2227.e5. [PubMed: 21864475]
25. Kindler HL, et al. Gemcitabine plus bevacizumab compared with gemcitabine plus placebo in patients with advanced pancreatic cancer: phase III trial of the Cancer and Leukemia Group B (CALGB 80303). J Clin Oncol. 2010; 28:3617–3622. [PubMed: 20606091]
26. Chen B, Pogue BW, Hoopes PJ, Hasan T. Combining vascular and cellular targeting regimens enhances the efficacy of photodynamic therapy. Int J Radiat Oncol Biol Phys. 2005; 61:1216–1226. [PubMed: 15752904]
27. Fingar VH, et al. Analysis of acute vascular damage after photodynamic therapy using benzoporphyrin derivative (BPD). Br J Cancer. 1999; 79:1702–1708. [PubMed: 10206280]
28. Kurohane K, et al. Photodynamic therapy targeted to tumor-induced angiogenic vessels. Cancer Lett. 2001; 167:49–56. [PubMed: 11323098]
29. Schmidt-Erfurth U, Hasan T. Mechanisms of Action of Photodynamic Therapy with Verteporfin for the Treatment of Age-Related Macular Degeneration. Surv Ophthalmol. 2000; 45:195–214. [PubMed: 11094244]
30. Huggett MT, et al. Phase I/II study of verteporfin photodynamic therapy in locally advanced pancreatic cancer. Br J Cancer. 2014; 110:1698–1704. [PubMed: 24569464]
31. Kessel D, Luo Y. Photodynamic therapy: A mitochondrial inducer of apoptosis. Cell Death Differ. 1999; 6:28–35. [PubMed: 10200545]

32. Kessel D. Death pathways associated with photodynamic therapy. Med Laser Appl. 2006; 21:219–224. [PubMed: 19890442]
33. Duska LR, Hamblin MR, Miller JL, Hasan T. Combination photoimmunotherapy and cisplatin: effects on human ovarian cancer ex vivo. J Natl Cancer Inst. 1999; 91:1557–1563. [PubMed: 10491432]
34. Rizvi I, et al. Synergistic enhancement of carboplatin efficacy with photodynamic therapy in a three-dimensional model for micrometastatic ovarian cancer. Cancer Res. 2010; 70:9319–9328. [PubMed: 21062986]
35. Celli JP, Solban N, Liang A, Pereira SP, Hasan T. Verteporfin-based photodynamic therapy overcomes gemcitabine insensitivity in a panel of pancreatic cancer cell lines. Lasers Surg Med. 2011; 43:565–574. [PubMed: 22057484]
36. del Carmen MG, et al. Synergism of epidermal growth factor receptor-targeted immunotherapy with photodynamic treatment of ovarian cancer in vivo. J Natl Cancer Inst. 2005; 97:1516–1524. [PubMed: 16234565]
37. Hlatky L, Hahnfeldt P, Folkman J. Clinical application of antiangiogenic therapy: microvessel density, what it does and doesn't tell us. J Natl Cancer Inst. 2002; 94:883–893. [PubMed: 12072542]
38. Spring BQ, et al. Efficient measurement of total tumor microvascularity ex vivo using a mathematical model to optimize volume subsampling. J Biomed Opt. 2013; 18:096015.
39. Yakes FM, et al. Cabozantinib (XL184), a novel MET and VEGFR2 inhibitor, simultaneously suppresses metastasis, angiogenesis, and tumor growth. Mol Cancer Ther. 2011; 10:2298–2308. [PubMed: 21926191]
40. Chang SK, Rizvi I, Solban N. In vivo optical molecular imaging of vascular endothelial growth factor for monitoring cancer treatment. Clin Cancer Res. 2008; 14:4146–4153. [PubMed: 18593993]
41. Tardi P, et al. In vivo maintenance of synergistic cytarabine:daunorubicin ratios greatly enhances therapeutic efficacy. Leuk Res. 2009; 33:129–139. [PubMed: 18676016]
42. Dromi S, et al. Pulsed-high intensity focused ultrasound and low temperature-sensitive liposomes for enhanced targeted drug delivery and antitumor effect. Clin Cancer Res. 2007; 13:2722–2727. [PubMed: 17473205]
43. Sengupta S, et al. Temporal targeting of tumour cells and neovasculature with a nanoscale delivery system. Nature. 2005; 436:568–572. [PubMed: 16049491]
44. Spring BQ, et al. Selective treatment and monitoring of disseminated cancer micrometastases in vivo using dual-function, activatable immunoconjugates. Proc Natl Acad Sci USA. 2014; 111:E933–42. [PubMed: 24572574]
45. Cheng J, et al. Formulation of functionalized PLGA–PEG nanoparticles for in vivo targeted drug delivery. Biomaterials. 2007; 28:869–876. [PubMed: 17055572]
46. Nel AE, et al. Understanding biophysicochemical interactions at the nano–bio interface. Nat Mater. 2009; 8:543–557. [PubMed: 19525947]
47. Mastronarde DN. Automated electron microscope tomography using robust prediction of specimen movements. J Struct Biol. 2005; 152:36–51. [PubMed: 16182563]
48. Kremer JR, Mastronarde DN, McIntosh JR. Computer visualization of three-dimensional image data using IMOD. J Struct Biol. 1996; 116:71–76. [PubMed: 8742726]
49. Humphrey W, Dalke A, Schulten K. VMD: visual molecular dynamics. J Mol Graphics. 1996; 14:33–38.
50. Larson MG. Analysis of Variance. Circulation. 2008; 117:115–121. [PubMed: 18172051]

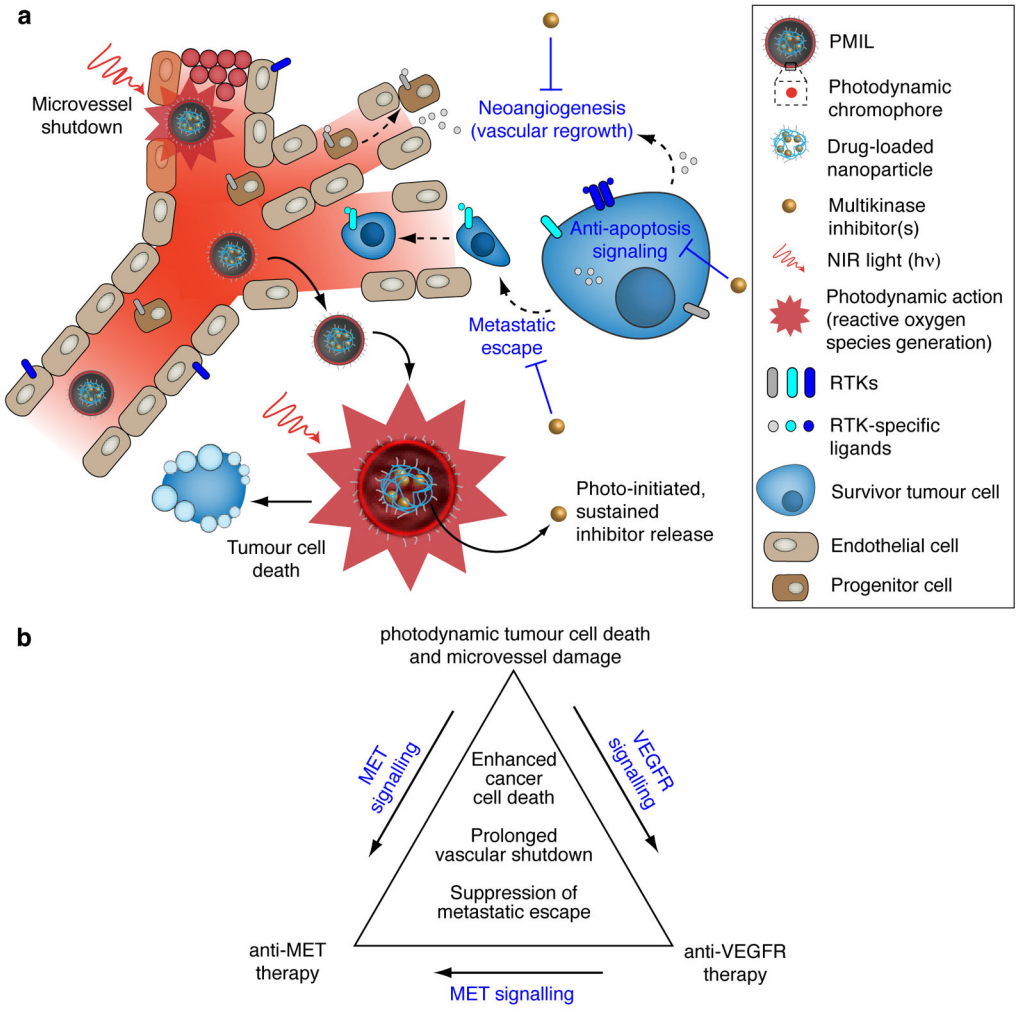

Figure 1. Concepts of spatiotemporal-synchronized combination therapy using PMILs

a, NIR light activates PMILs within the tumour microvasculature and parenchyma for simultaneous neovascular damage, tumour cell apoptosis and necrosis as well as liposome disruption with initiation of sustained multikinase inhibition. The PMIL delivery system is tuneable for simultaneous delivery of photodynamic, chemotherapeutics and small-molecular inhibitors. **b,** Schematic of a three-way interactive combination therapy with photodynamic tumour cell and microvasculature damage and inhibition of treatment escape pathways. VEGFR signalling stimulates tumour angiogenesis and preparation of the premetastatic niche via supporting endothelial cell survival, migration and proliferation as well as increased vessel permeability and chemotaxis of bone marrow derived progenitor cells. MET signalling promotes escape from cytotoxic and antiangiogenic therapy via supporting cancer cell survival, motility and metastasis as well as cancer stem-like cell maintenance and tumour angiogenesis via cross talk with the VEGFR pathway. XL184 inhibits activation of both the MET and VEGF signalling pathways to suppress tumour cell survival, metastasis and regrowth following cytotoxic therapy.

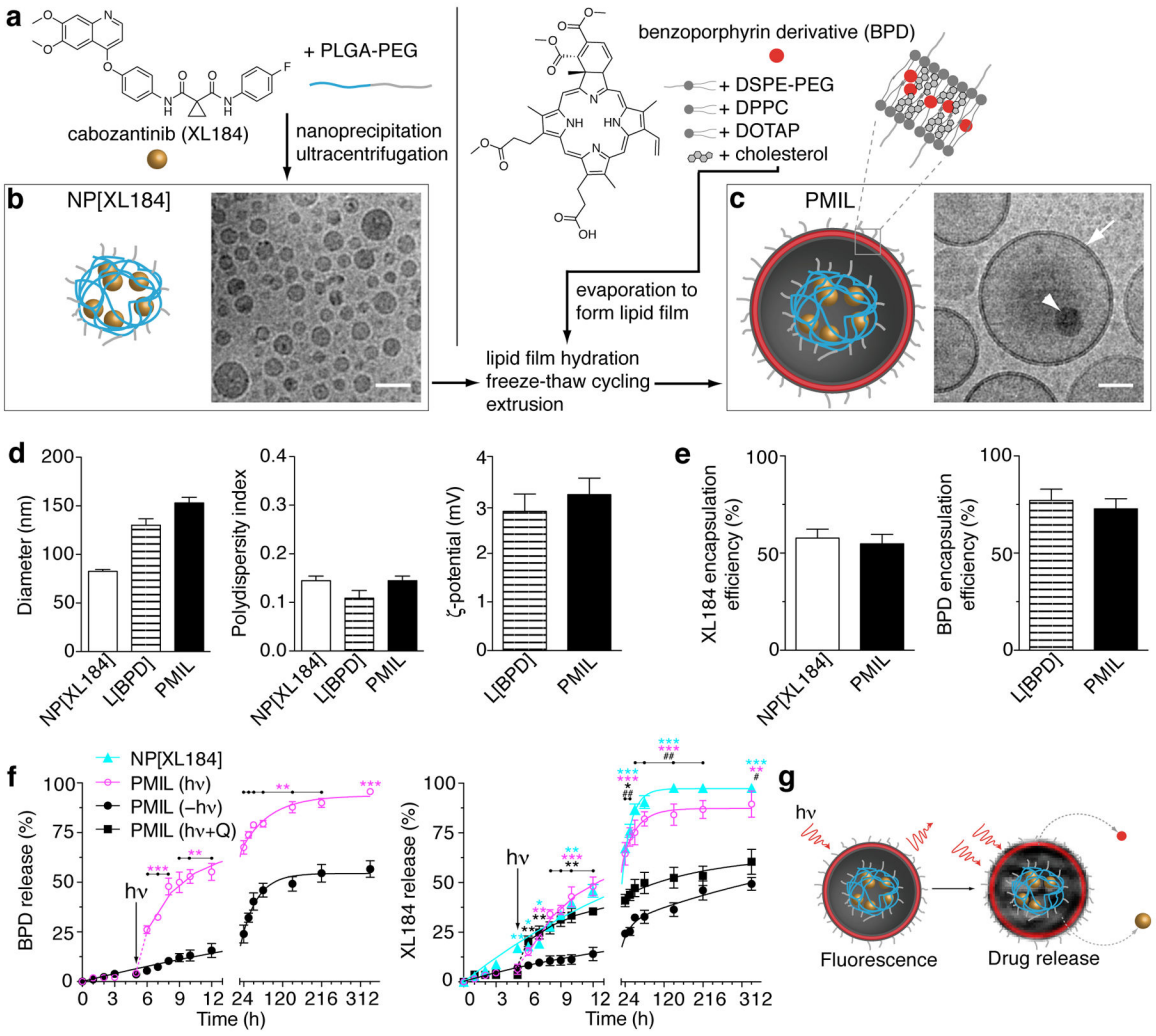

Figure 2. Synthesis and characterization of a benzoporphyrin–XL184 PMIL

a, Diagrams of XL184-loaded nanoparticle (NP[XL184]) and BPD-loaded lipid film synthesis. DOTAP, 1,2-dioleoyl-3-trimethylammonium-propane; DPPC, 1,2-dipalmitoly-sn-glycero-3-phosphocholine; DSPE-PEG, 1,2-distearoyl-sn-glycero-3-phosphoethanolamine-N-[methoxy(polyethylene glycol)200]; PLGA-PEG, poly-(lactic acid-co-glycolic) acid–polyethylene glycol conjugate. Schematics and representative cryo-electron microscopy (cryo-EM) images of, **b**, NP[XL184] and, **c**, PMIL. Arrows and arrowheads indicate the outer lipid bilayer and an encapsulated nanoparticle, respectively, in **c**. Scale bars, 50 nm. **d**, Physical characterization of the various nanoconstructs by dynamic light scattering, and, **e**, nanoconstruct drug encapsulation efficiencies. Results are mean ± s.e.m. (NP[XL184] and PMIL, $n = 12$ technical replicates each performed with an independent nanomaterial preparation; L[BPD], $n = 10$ technical replicates each performed with an independent nanomaterial preparation). **f**, Photo-induced drug release from PMILs in serum versus release in the absence of laser irradiation. The arrows in **f** indicate that a NIR light dose was given at the 5 h time point (37°C; 100 mW·cm^{-2}; 5 J·cm^{-2}). Results are mean ± s.e.m. ($n = 3$ technical replicates each performed with an independent nanomaterial preparation; error is

small where not visible). Asterisks and hashes in **f** denote significance compared to untreated PMILs (PMIL, −hν) or NIR-irradiated PMILs (PMIL, hν) compared to NIR-irradiated PMILs in the presence of sodium azide (a reactive oxygen species scavenger; PMIL, hν+Q), respectively (*,# $P<0.05$, **,## $P<0.01$, *** $P<0.001$, one-way ANOVA with Tukey's post-hoc test). Trend lines are fits to a simple one- or two-phase exponential release model (*Methods*). **g**, Schematic of PMIL fluorescence imaging and photo-induced drug release.

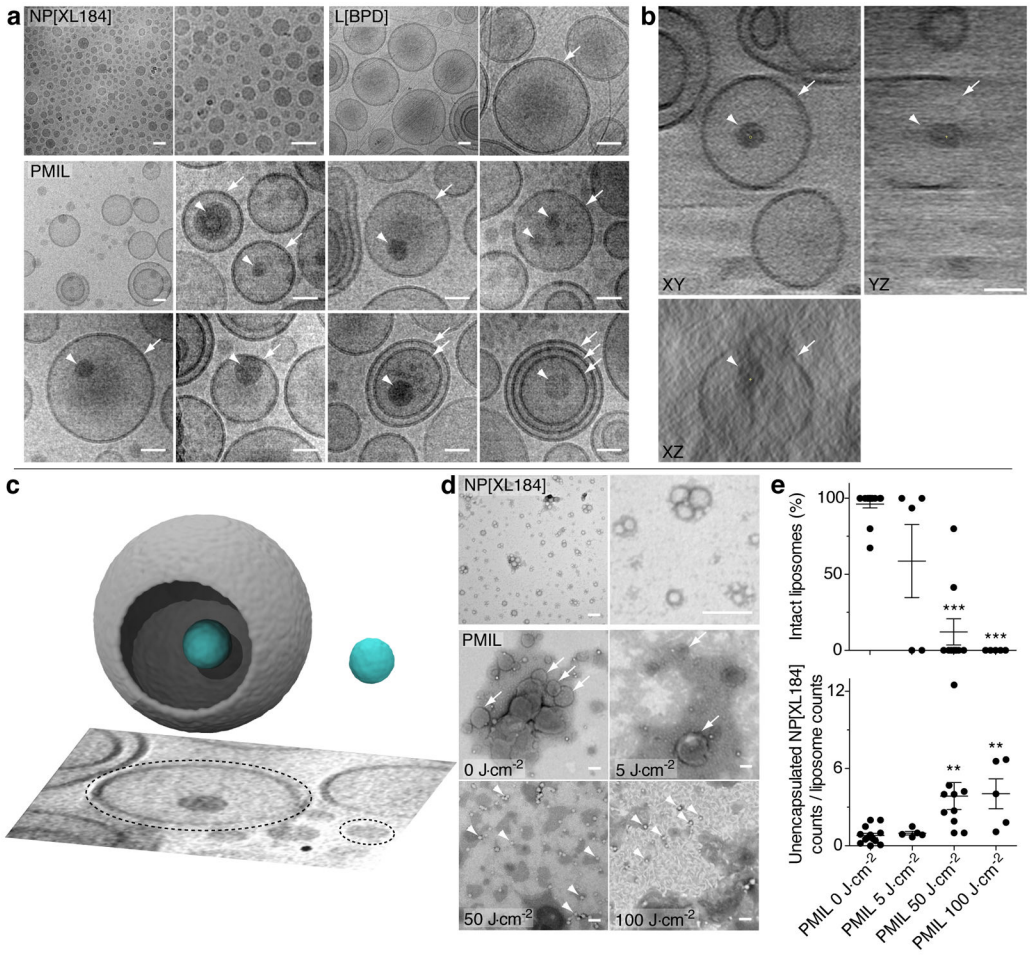

Figure 3. Structural imaging of NP[XL184] encapsulation and XL184 photo-release from PMILs

a, Representative cryo-EM images of NP[XL184], L[BPD] and PMIL. **b**, Cryo-EM tomogram of a PMIL. Arrows and arrowheads in **a** and **b** indicate the outer lipid bilayer and encapsulated nanoparticles, respectively. Scale bars, 50 nm. Empty liposomes, unencapsulated NP[XL184] and multilamellar liposomes were also observed in the PMIL samples (Supplementary Fig. 5a–c and Supplementary Note 3). **c**, 3D renders of an exemplary PMIL encapsulating a nanoparticle as well as an exemplary unencapsulated nanoparticle from a cryo-EM tomogram of a PMIL sample. The dashed circles indicate the rendered objects in the lower 2D tomogram slice. **d**, Representative transmission electron microscopy (TEM) images of NP[XL184] and PMIL treated with varying NIR light doses (100 mW·cm^{-2}; 0, 5, 50, or 100 J·cm^{-2}), and using negative staining with phosphotungstic acid. Arrows and arrowheads indicate intact liposomes and unencapsulated nanoparticles, respectively. Scale bars, 100 nm. **e**, Quantification of intact liposomes and unencapsulated nanoparticles shown in **d** (Supplementary Fig. 5e). Results are mean ± s.e.m. Asterisks in **e** denote significance compared to untreated PMILs, 0 J·cm^{-2} (PMIL 0 J·cm^{-2}, n = 14 images; PMIL 5 J·cm^{-2}, n = 5 images; PMIL 50 J·cm^{-2}, n = 10 images; PMIL 100 J·cm^{-2}, n = 5 images; the images were collected from two technical replicates performed with a single

nanomaterial preparation for each group; $^{**}P<0.01$, $^{***}P<0.001$, Kruskal-Wallis one-way ANOVA).

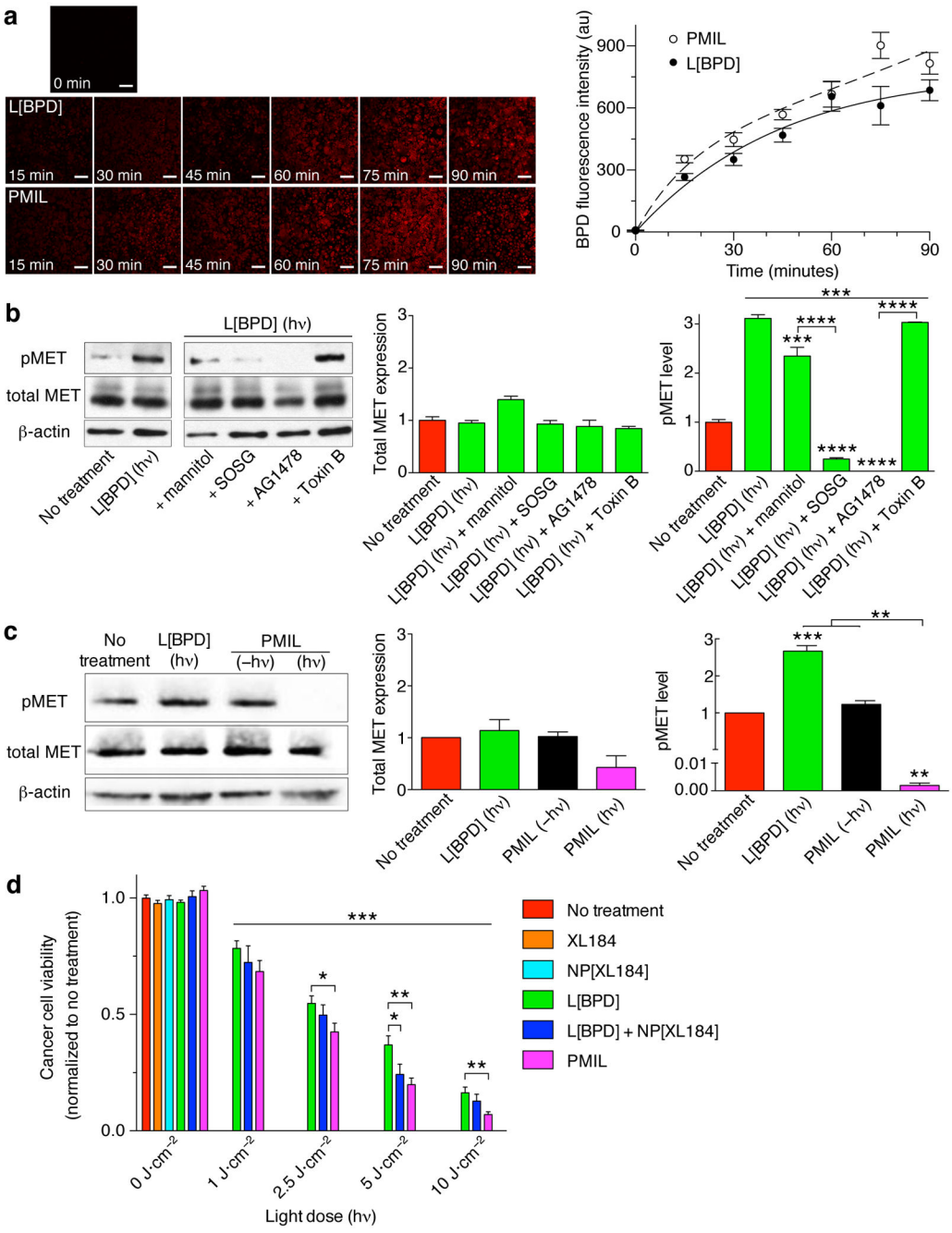

Figure 4. MET inhibition enhances PDT-induced cancer cell death *in vitro* using PMILs

a, Representative confocal BPD fluorescence microscopy images and quantification of BPD fluorescence during L[BPD] and PMIL cellular uptake in monolayer AsPC1 cell cultures. Results are mean ± s.e.m. (n = 3 biological replicates per condition × 3 images per replicate). Trend lines are fits to a simple pharmacokinetic model (*Methods*). **b**, Western blotting and quantification of total MET and pMET expression—normalized to β-actin and relative to the no-treatment control group (normalized to 1)—indicate that pMET increases 24 h following PDT with L[BPD] (L[BPD]-PDT; 125 nM BPD; 690 nm; 100 mW·cm^{-2}; 2.5

J·cm^{-2}), whereas there is no significant change in overall MET protein expression following PDT over a range of PDT doses (Supplementary Fig. 6). A singlet oxygen-specific scavenger (Singlet Oxygen Sensor Green, SOSG; 100 μM) inhibits L[BPD]-PDT activation of MET signalling, whereas a free radical scavenger (mannitol, 50 mM) has only a modest affect. In addition, an EGFR-specific kinase inhibitor, AG1478 (12.5 nM), also inhibits MET activation following PDT whereas toxin B (2 ng/mL), an inhibitor of GPCR-mediated MET transactivation, has no effect. Results are mean ± s.e.m. Underlined asterisks denote significance compared to no treatment, and the remaining asterisks denote significance compared to L[BPD]-PDT, L[BPD] (h ν), or amongst the indicated groups (n = 3 biological replicates per condition; ***P <0.001, ****P <0.0001, one-way ANOVA with Tukey's post-hoc test). **c**, Western blots and quantification of photo-induced suppression of MET activation (pMET) using PMILs 24 h following treatment. In contrast to increased pMET following L[BPD]-PDT, MET activation is suppressed following PDT with PMILs (250 nM BPD; 690 nm; 100 mW·cm^{-2}; 1 J·cm^{-2}). Without photo-induced XL184 release (PMIL, −hν), the PMIL has no affect on basal levels of pMET. Results are mean ± s.e.m. (n = 2 biological replicates per condition; **P <0.01, ***P <0.001, one-way ANOVA with Tukey's post-hoc test). **d**, MTT assay of AsPC1 cell viability following XL184 and PDT monotherapy or combination therapy. Results are mean ± s.e.m. Asterisks denote significance compared to no treatment or amongst the indicated groups (No-treatment control and L[BPD] 0 J·cm^{-2}, n = 17 biological replicates; XL184, n = 10 biological replicates; NP[XL184], n = 16 biological replicates; L[BPD]+NP[XL184] 0 and 1 J·cm^{-2}, n = 5 biological replicates; L[BPD] 1 J·cm^{-2}, L[BPD]+NP[XL184] 2.5, 5 and 10 J·cm^{-2}, PMIL 0 and 1 J·cm^{-2}, n = 8 biological replicates; L[BPD] 2.5, 5 and 10 J·cm^{-2}, and PMIL 2.5, 5 and 10 J·cm^{-2}, n = 11 biological replicates; *P <0.05, **P <0.01, ***P <0.001, one-way ANOVA with Tukey's post-hoc test). Fisher's least significant difference post-hoc test of the integrated PDT dose response curves (analysis of the area under the curve mean and standard error) indicates that the PMIL achieves enhanced cancer cell death versus L[BPD] + NP[XL184] (P <0.05) and L[BPD] (P <0.001) (Supplementary Fig. 7a).

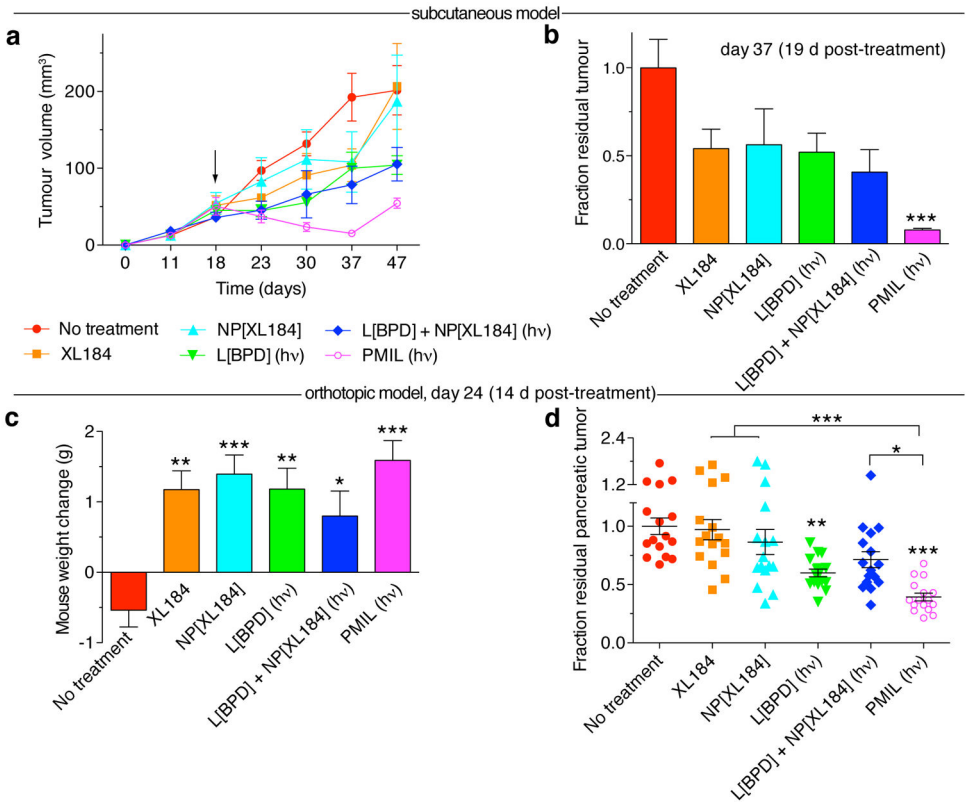

Figure 5. Prolonged tumour reduction *in vivo* with a single cycle of PMIL-treatment

Combined BPD-PDT (690 nm; 100 mW·cm^{-2}; 75 J·cm^{-2}) and XL184 treatment using PMILs achieves, **a**, prolonged reductions in subcutaneous tumour volumes, **b**, with a minimal fractional residual tumour on day 37. The arrow in **a** indicates administration of a single treatment cycle. Results are mean ± s.e.m. Error is small where hidden. Asterisks in **b** denote significance compared to no treatment (n = 5 mice per group; ***P = 0.0038, Kruskal-Wallis one-way ANOVA). Orthotopic PDAC mouse, **c**, weight change (compared to 10 d posttumour inoculation, prior to treatment) and, **d**, pancreatic tumour volume at the experiment endpoint (37 d following tumour inoculation). Results are mean ± s.e.m. Asterisks denote significance compared to no treatment or amongst the indicated groups (n = 16 mice per group; *P <0.05, **P <0.01, ***P <0.001, Kruskal-Wallis one-way ANOVA). A single cycle of combination therapy using PMILs achieves enhanced reductions in orthotopic tumours (P = 0.011, two-way ANOVA BPD-PDT·XL184 interaction term; Supplementary Fig. 7b and Supplementary Tables 1 and 2)—but not using the conventional combination, L[BPD] + NP[XL184] (P = 0.23).

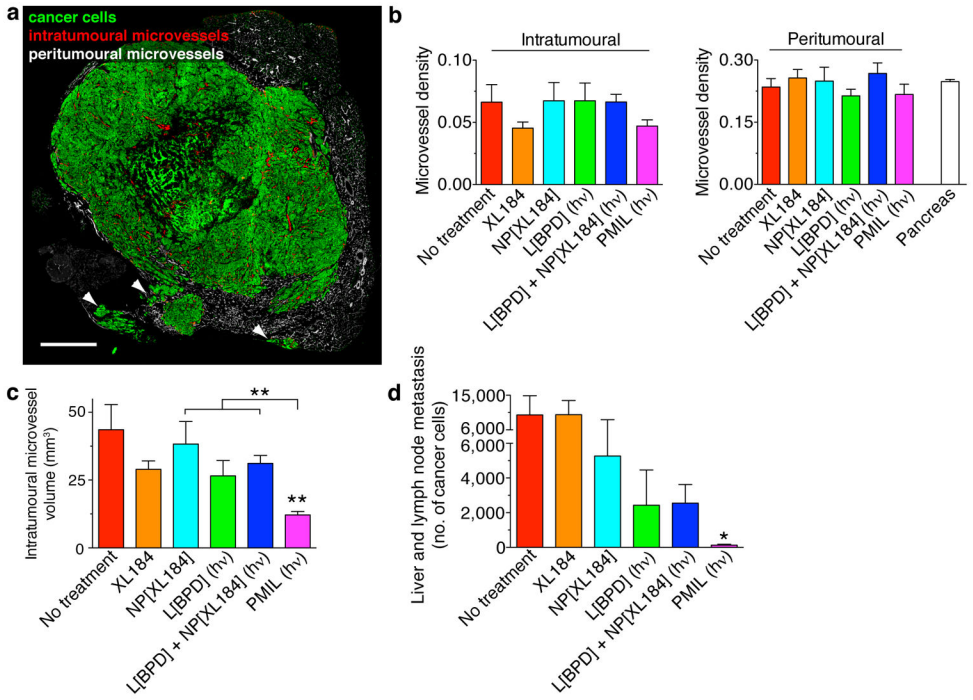

Figure 6. Antivascular and antimetastatic effects using a single PMIL-treatment cycle *in vivo*

a, A representative confocal fluorescence image mosaic of an entire orthotopic PDAC tumour cross-section with 1.2 μm x–y sampling illustrates selective immunostaining of human epithelial cancer cells (green) to discriminate intra- (red) and peritumoural (gray scale) endothelial cells. Arrows indicate local metastases and cancer cells infiltrating the surrounding pancreatic tissue. Scale bar, 1 mm. **b**, Intra- and peritumoural microvessel densities at the treatment endpoint. **c**, A single PMIL-treatment induces a decrease in intratumoural microvessel volume. Results are mean ± s.e.m. Asterisks denote significance compared to no treatment or amongst the indicated groups (no-treatment control, $n = 8$ entire tumour cross-section image mosaics from 8 mice; XL184, $n = 7$ entire cross-sections from 3 mice; NP[XL184], $n = 8$ entire cross-sections from 4 mice; L[BPD], 8 entire cross-sections from 4 mice; L[BPD]+NP[XL184], 10 entire cross-sections from 5 mice; PMIL, 10 entire cross-sections from 7 mice; $^{**}P < 0.01$, Kruskal-Wallis one-way ANOVA). **d**, A single PMIL-treatment reduces the number of total number of metastatic cancer cells in the liver and regional lymph nodes. Results are mean ± s.e.m. Asterisks denote significance compared to no treatment (no-treatment control, NP[XL184], L[BPD]+NP[XL184], and PMIL, $n = 20$ mice per group; XL184, $n = 18$ mice; L[BPD], $n = 16$ mice; $^{*}P < 0.05$, Kruskal-Wallis one-way ANOVA).